ActaDV

Acta Dermato-Venereologica

Advances in dermatology and venereology

Differentiation Between Benign and Malignant Pigmented Skin Tumours Using Bedside Diagnostic Imaging Technologies: A Pilot Study

Terese VON KNORRING[1], Niels MØLLER ISRAELSEN[2,3], Vilde UNG[4], Julie L. FORMANN[4], Mikkel JENSEN[2,3], Merete HAEDERSDAL[1], Ole BANG[2,3], Gabriella FREDMAN[1] and Mette MOGENSEN[1]

[1]Department of Dermatology, Copenhagen University Hospital, Bispebjerg and Frederiksberg, Copenhagen, [2]DTU Fotonik, Department of Photonics Engineering, Technical University of Denmark, Kongens Lyngby, [3]NKT Photonics A/S, Birkerød, and [4]Department of Public Health, Section of Biostatistics, University of Copenhagen, Copenhagen, Denmark

Rapid diagnosis of suspicious pigmented skin lesions is imperative; however, current bedside skin imaging technologies are either limited in penetration depth or resolution. Combining imaging methods is therefore highly relevant for skin cancer diagnostics. This pilot study evaluated the ability of optical coherence tomography, reflectance confocal microscopy, photoacoustic imaging and high-frequency ultrasound to differentiate malignant from benign pigmented skin lesions. A total of 41 pigmented skin tumours were scanned prior to excision. Morphological features and blood vessel characteristics were analysed with reflectance confocal microscopy, optical coherence tomography, high-frequency ultrasound and photoacoustic imaging images, and the diagnostic accuracy was assessed. Three novel photoacoustic imaging features, 7 reflectance confocal microscopy features, and 2 optical coherence tomography features were detected that had a high correlation with malignancy; diagnostic accuracy >71%. No significant features were found in high-frequency ultrasound. In conclusion, optical coherence tomography, reflectance confocal microscopy and photoacoustic imaging in combination enable image-guided bedside evaluation of suspicious pigmented skin tumours. Combining these advanced techniques may enable more efficient diagnosis of skin cancer.

SIGNIFICANCE

Pigmented tumours can have extremely similar clinical appearance, but very different prognostic implications. Typically, surgical excision is recommended for suspicious lesions, but advanced skin imaging technologies create new opportunities for rapid non-invasive image-guided diagnosis of skin cancer. This study combined 4 skin imaging technologies at the bedside in a single session. This article presents the most important image-based diagnostic features and reports moderate diagnostic accuracies for each device. The combination of advanced imaging technologies may assist in the diagnosis of pre-surgical skin cancer and reduce the delay from diagnosis to treatment of suspicious pigmented lesions.

A ccurate preoperative evaluation of suspicious pigmented skin lesions is important, since it may reduce the number of unnecessary surgical excisions (1, 2). Several non-invasive skin imaging technologies have become commercially available in recent years, thereby creating a new opportunity for image-guided diagnosis. These include *in vivo* reflectance confocal microscopy (RCM), optical coherence tomography (OCT), and photoacoustic imaging (PAI) (1, 3–7). High-frequency ultrasound (HFUS) has been available for decades.

Bedside imaging technologies all have their strengths and limitations, mainly related to a trade-off between penetration depth and resolution. Consequently, the obvious ideal diagnostic strategy would be to combine various imaging methods, which is the core aim of this study. HFUS can provide important information on tumour thickness required for pre-surgical planning (8, 9). RCM is a laser-based microscopy technology that enables *in vivo* horizontal scanning at cellular resolution (10). OCT utilizes near-infrared light to create real-time cross-section images of the skin, resulting in higher resolution than ultrasonography and deeper penetration than RCM (11–13). In addition to visualizing skin architecture, the use of the angiographic OCT (OCTA) technique enables visualization of red superficial blood vessels superimposed on greyscale OCT images (14). OCT has shown promising results in several studies as a bedside tool for the diagnosis and margin delineation of, especially, BCC (15–17). Photoacoustic imaging (PAI), also termed multispectral optoacoustic tomography (MSOT), combines the contrast of optical imaging with the spatial resolution of ultrasound (18), using melanin and haemoglobin as endogenous contrast agents. PAI has a unique ability to visualize deep skin structures at centimetre-level depth, as well as blood flow in skin vasculature, which is not achievable with other non-invasive technologies, and has

shown promising results regarding skin tumour diagnosis, delineation, and vascular visualization (18–21).

This pilot study combined all 4 imaging technologies: HFUS, RCM, OCT and PAI, for the bedside diagnosis of suspicious pigmented skin lesions, in a single session. The study aims to explore image-guided evaluation of diagnostic features in pigmented lesions, and to evaluate the potential to differentiate malignant from benign lesions at first patient visit, by assessing and comparing diagnostic accuracies of the various methods. The complementary effects of using multiple devices for the bedside diagnosis of skin cancer is explored, and its future potential estimated for triaging patients into excision or topical treatment vs no treatment, based on diagnostic accuracy measures obtained in a single session. Tumour thickness was measured with PAI, OCT and HFUS.

MATERIALS AND METHODS

Study design and patient recruitment

This prospective non-blinded clinical trial was carried out under a protocol approved by the local ethics committee (H-19036900) and by the Danish Medicines Agency, Medical Devices section (CIV-19-05-028648) and registered at ClinTrials.gov (NCT04229277). Written consent was obtained before enrolment in the study in accordance with the Declaration of Helsinki. From 1 to 15 March 2020, patients with pigmented skin lesions were enrolled at Department of Dermatology, Bispebjerg Hospital, Copenhagen.

All patients were scanned by an experienced dermatologist in a 20–35-min session, with all imaging techniques, in the same room. Prior to scanning, dermoscopy images were obtained. Lesions that were only lightly pigmented were included if patients reported significant growth or changes over time. Patients were scanned with 4 different imaging technologies, including 5 modalities: HFUS, 2 different OCT systems, RCM and PAI. Technical descriptions of each imaging modality are shown in Appendix S1. The images were saved in a digital archiving system for subsequent scoring and further evaluation. After imaging, a skin-punch biopsy or excisional biopsy was performed and sent for conventional histopathology analysis by a dermatopathologist.

Assessment of optical coherence tomography, reflectance confocal microscopy, photoacoustic imaging and high-frequency ultrasound images

Two authors (MM and GF), blinded to histopathology results, evaluated the presence or absence of predetermined morphological features and blood vessel characteristics associated with malignant or benign lesions in images obtained from 2 OCT systems, HFUS and PAI. When the 2 assessors did not agree on image features (3/41 cases) a re-analysis of images was performed together, and consensus was obtained (41/41). Author MM assessed all RCM features, since she is the only confocal microscopy expert in the department. The study data set thus does not allow intra- and inter-observer agreement analysis. Annotated features were identified from literature research (19–27) and a few novel features were introduced based on the authors' previous clinical experiences. All features are shown in **Table I**. Novel features not previously described in the literature are outlined with an asterisk. Features found in each type of lesion are outlined in Table SI, divided into malignant lesions including malignant melanoma (MM), basal cell carcinomas (BCC), squamous cell carcinomas (SCC), potentially malignant lesions, such as atypical naevi (AN) with epidermal me-

lanocytic proliferation and premalignant actinic keratosis (AK); and benign lesions include naevus (N) and seborrhoeic keratosis (SK).

Diagnostic accuracy for each parameter, listed in Table I, was calculated as the ability to discriminate between benign and malignant lesions. Premalignant lesions (AK) and potentially malignant lesions (AN) were considered malignant in diagnostic accuracy calculation. It is possible that most lesions currently reported as naevi with atypical intraepidermal melanocytic proliferation (AIMP) are, in fact, benign, and that their significance lies in the potential pitfall for overdiagnosis of malignant melanoma. However, this pilot study included AN in the malignant category, since studies have shown that up to 20% of these lesions are diagnosed as melanoma *in situ* (MIS) in pathology revisions (28). Furthermore, it has been demonstrated previously in a retrospective study that the risk of evolution to MIS in AIMP lesions is higher in lesions that demonstrate a high number of dendritic cells touching each other in RCM images (28). Consequently, malignant lesions included: MM, BCC, SCC, AN and AK, while benign lesions included N, SK and others (see Table SI).

Image-guided findings were compared with histopathological diagnosis, which was considered a reference standard. Tumour thickness was measured with PAI, OCT and HFUS images and was not correlated with histopathology.

Outcome measures

Diagnostic features were divided into morphological features, related to characteristics of cells, overall skin architecture, and melanin content and distribution inside the lesion, only accessible in PAI images; and blood vessel characteristics, related to size and structure of blood vessels in angiographic OCT images and molecular contrast from oxygenated HbO_2 and deoxygenized Hb in PAI (Table I).

Sample sizes were initially considered too small to evaluate diagnostic accuracy for individual lesion types. Blood vessel morphology was assessed and classified according to diameter and location inside or outside the tumour. A secondary outcome was tumour thickness (in mm) from the skin surface to the deepest part of the tumour in a vertical direction with OCT, PAI and HFUS.

Statistical analysis

No power calculation was performed for this explorative pilot study. Descriptive statistics are numbers and percentages for categorical data, and medians and quartiles for continuous data. The diagnostic performance of binary predictors was summarized by sensitivity, specificity, and diagnostic accuracy with exact binomial 95% confidence intervals (95% CI).

The diagnostic performance of continuous predictors was summarized as area under the curve (AUC) with cross-validated 95% CI. *p*-values were computed for the null hypothesis: diagnostic accuracy 0.5. To guard against spurious findings, all p-values were corrected for multiple testing using the method of Benjamini and Hochberg, which controls false discovery rate (29). An adjusted *p*-value < 0.05 was considered statistically significant. Only adjusted *p*-values (*p*-adjusted) are reported.

RESULTS

Patient demographics and histopathology

A total of 41 pigmented skin lesions from 41 patients underwent imaging, and were consecutively included in the study over 2 weeks, corresponding to 25 women and 16 men, mean age 52 years (range 21–85 years), Fitzpatrick skin type I: *n* = 2, II: *n* = 35, III: *n* = 3, and IV:

Table I. Ability to differentiate between benign and malignant lesions. All evaluated high-frequency ultrasound (HFUS), photoacoustic imaging (PAI), reflectance confocal microscopy (RCM) and optical coherence tomography (OCT) features presented, with sensitivity, specificity, and diagnostic accuracy

Features evaluated	Sensitivity (95% CI)	Specificity (95% CI)	Diagnostic accuracy (95% CI)/AUC (95% CI)	Adjusted *p*-value
HFUS morphology				
Dark hypoechogenic areas	1 (0.78, 1)	0.04 (0, 0.2)	0.39 (0.24, 0.55)	0.36
HFUS blood vessels				
Outside tumour Doppler	0.64 (0.35, 0.87)	0.42 (0.23, 0.63)	0.5 (0.34, 0.66)	1
Inside tumour Doppler	0.36 (0.13, 0.65)	0.58 (0.37, 0.77)	0.5 (0.34, 0.66)	1
PAI morphology				
MELANIN dense superficial *	0.85 (0.55, 0.98)	0.04 (0, 0.2)	0.31 (0.17, 0.48)	0.08
MELANIN shell-like areas in epidermis*	0.08 (0, 0.36)	0.77 (0.56, 0.91)	0.54 (0.37, 0.7)	0.83
MELANIN diffuse deep pigmentation*	0.62 (0.32, 0.86)	0.58 (0.37, 0.77)	0.59 (0.42, 0.74)	0.49
MELANIN blood vessels inside melanin area*	0.77 (0.46, 0.95)	0.58 (0.37, 0.77)	0.64 (0.47, 0.79)	0.23
PAI blood vessels				
Hb inside tumour	**0.54 (0.25, 0.81)**	**0.77 (0.56, 0.91)**	0.69 (0.52, 0.83)	0.08
Hb increased diameter	**0.38 (0.14, 0.68)**	**0.92 (0.75, 0.99)**	**0.74 (0.58, 0.87)**	**0.02**
Hb outside tumour	1 (0.75, 1)	0.08 (0.01, 0.25)	0.38 (0.23, 0.55)	0.36
HbO$_2$ inside tumour	**1 (0.75, 1)**	**0.62 (0.41, 0.8)**	**0.74 (0.58, 0.87)**	**0.02**
HbO$_2$ increased diameter	0.69 (0.39, 0.91)	0.42 (0.23, 0.63)	0.51 (0.35, 0.68)	1
HbO$_2$ outside tumour	0.92 (0.64, 1)	0 (0, 0.13)	0.31 (0.17, 0.48)	0.08
RCM morphology				
Pagetoid cells	0.13 (0.02, 0.4)	1 (0.87, 1)	0.68 (0.52, 0.82)	0.08
Pagetoid spread (dendritic & round)	**0.4 (0.16, 0.68)**	**0.92 (0.75, 0.99)**	**0.73 (0.57, 0.86)**	**0.02**
Atypical melanocytes inside adnexa	**0.2 (0.04, 0.48)**	**1 (0.87, 1)**	**0.71 (0.54, 0.84)**	**0.04**
Dendritic cells	0.6 (0.32, 0.84)	0.65 (0.44, 0.83)	0.63 (0.47, 0.78)	0.23
Abnormal dendritic cells	0.27 (0.08, 0.55)	0.88 (0.7, 0.98)	0.66 (0.49, 0.8)	0.15
Inflammatory cells	0.33 (0.12, 0.62)	0.73 (0.52, 0.88)	0.59 (0.42, 0.74)	0.49
Melanophages/bright cells	0.87 (0.6, 0.98)	0.12 (0.02, 0.3)	0.39 (0.24, 0.55)	0.36
Regular honeycomb	**0.47 (0.21, 0.73)**	**0.08 (0.01, 0.25)**	**0.22 (0.11, 0.38)**	**0.01**
Atypical dysplastic honeycomb	**0.67 (0.38, 0.88)**	**0.81 (0.61, 0.93)**	**0.76 (0.6, 0.88)**	**0.02**
Cobblestone pattern DEJ	0.33 (0.12, 0.62)	0.62 (0.41, 0.8)	0.51 (0.35, 0.67)	1
Junctional disarray	0.53 (0.27, 0.79)	0.69 (0.48, 0.86)	0.63 (0.47, 0.78)	0.23
Non-edged papillae	**0.47 (0.21, 0.73)**	**0.85 (0.65, 0.96)**	**0.71 (0.54, 0.84)**	**0.04**
Medusa head	**0.13 (0.02, 0.4)**	**1 (0.87, 1)**	0.68 (0.52, 0.82)	0.08
Cordlike cell aggregations in dermis	**0.4 (0.16, 0.68)**	**0.92 (0.75, 0.99)**	**0.73 (0.57, 0.86)**	**0.02**
Nucleated cells in dermal papillae	**0.4 (0.16, 0.68)**	**0.92 (0.75, 0.99)**	**0.73 (0.57, 0.86)**	**0.02**
Regular ringed/edged papillae DEJ	0.33 (0.12, 0.62)	0.5 (0.3, 0.7)	0.44 (0.28, 0.6)	0.68
Sparse hyper-reflective nests DEJ	0.27 (0.08, 0.55)	0.69 (0.48, 0.86)	0.54 (0.37, 0.69)	0.83
Dense hyper-reflective nests/clod DEJ	0.2 (0.04, 0.48)	0.85 (0.65, 0.96)	0.61 (0.45, 0.76)	0.36
Dense fenestrated pattern of collagen*	0.27 (0.08, 0.55)	0.69 (0.48, 0.86)	0.54 (0.37, 0.69)	0.83
Dermal component of refractive cells	0.53 (0.27, 0.79)	0.58 (0.37, 0.77)	0.56 (0.4, 0.72)	0.68
Peritumoural dark clefting	**0.2 (0.04, 0.48)**	**1 (0.87, 1)**	**0.71 (0.54, 0.84)**	**0.04**
Peripheral palisading	**0.27 (0.08, 0.55)**	**1 (0.87, 1)**	**0.73 (0.57, 0.86)**	**0.02**
Dark islands	**0.27 (0.08, 0.55)**	**1 (0.87, 1)**	**0.73 (0.57, 0.86)**	**0.02**
Cauliflower-like lesions	**0.27 (0.08, 0.55)**	**1 (0.87, 1)**	**0.73 (0.57, 0.86)**	**0.02**
Streaming	**0.27 (0.08, 0.55)**	**1 (0.87, 1)**	**0.73 (0.57, 0.86)**	**0.02**
PPC	0.27 (0.08, 0.55)	0.77 (0.56, 0.91)	0.59 (0.42, 0.74)	0.49
Solar elastosis	0.07 (0, 0.32)	0.96 (0.8, 1)	0.63 (0.47, 0.78)	0.23
RCM blood vessels				
Inside tumour	0.73 (0.45, 0.92)	0.54 (0.33, 0.73)	0.61 (0.45, 0.76)	0.36
Arborizing vessels in tumour	**0.4 (0.16, 0.68)**	**1 (0.87, 1)**	**0.78 (0.62, 0.89)**	**0.01**
Enlarged diameter	0.67 (0.38, 0.88)	0.62 (0.41, 0.8)	0.63 (0.47, 0.78)	0.23
Chaotic vessels	0.07 (0, 0.32)	0.96 (0.8, 1)	0.63 (0.47, 0.78)	0.23
UHR-OCT morphology				
DEJ visible	0.25 (0.05, 0.57)	0.74 (0.49, 0.91)	0.55 (0.36, 0.73)	0.83
Ovoid dark areas	0.25 (0.05, 0.57)	0.95 (0.74, 1)	0.68 (0.49, 0.83)	0.17
Dark nests	0.58 (0.28, 0.85)	0.32 (0.13, 0.57)	0.42 (0.25, 0.61)	0.65
White halo	0.08 (0, 0.38)	0.95 (0.74, 1)	0.61 (0.42, 0.78)	0.44
Clefting	0.25 (0.05, 0.57)	1 (0.82, 1)	0.71 (0.52, 0.86)	0.08
Bright nests	0.33 (0.1, 0.65)	0.68 (0.43, 0.87)	0.55 (0.36, 0.73)	0.83
Hyper-reflective columns	0.5 (0.21, 0.79)	0.58 (0.33, 0.8)	0.55 (0.36, 0.73)	0.83
Round keratin dots	0 (0, 0.26)	0.63 (0.38, 0.84)	0.39 (0.22, 0.58)	0.44
White streaks/granules	0.42 (0.15, 0.72)	0.37 (0.16, 0.62)	0.39 (0.22, 0.58)	0.44
Marble-like epidermis*	0.5 (0.21, 0.79)	0.26 (0.09, 0.51)	0.35 (0.19, 0.55)	0.29
C-OCT and OCTA morphology				
OCTA dotted vessels at 0,15 mm*	0.6 (0.32, 0.84)	0.35 (0.17, 0.56)	0.44 (0.28, 0.6)	0.68
OCTA vessel mesh at 0,50 mm*	0.2 (0.04, 0.48)	0.54 (0.33, 0.73)	0.41 (0.26, 0.58)	0.49
Ovoid dark areas	**0.27 (0.08, 0.55)**	**0.96 (0.8, 1)**	**0.71 (0.54, 0.84)**	**0.04**
Dark nests	0.73 (0.45, 0.92)	0.42 (0.23, 0.63)	0.54 (0.37, 0.69)	0.83
White halo	0.07 (0, 0.32)	1 (0.87, 1)	0.66 (0.49, 0.8)	0.15
Clefting	**0.27 (0.08, 0.55)**	**1 (0.87, 1)**	**0.73 (0.57, 0.86)**	**0.02**
Bright nests	0.27 (0.08, 0.55)	0.65 (0.44, 0.83)	0.51 (0.35, 0.67)	1
Hyper-reflective columns	0.33 (0.12, 0.62)	0.73 (0.52, 0.88)	0.59 (0.42, 0.74)	0.49
Round keratin dots	0.07 (0, 0.32)	0.81 (0.57, 0.93)	0.54 (0.37, 0.69)	0.83
Ice peaks	0.07 (0, 0.32)	1 (0.87, 1)	0.66 (0.49, 0.8)	0.15
White streaks in epidermis	0.2 (0.04, 0.48)	0.68 (0.46, 0.85)	0.5 (0.34, 0.66)	1
Marble-like epidermis*	0.4 (0.16, 0.68)	0.65 (0.44, 0.83)	0.56 (0.4, 0.72)	0.68
OCTA blood vessels	Median	Median		
Plexus depth (µm)	275	289	0.59 (0.4, 0.59)	0.61
Vessel diameter (µm)	48	44	0.57 (0.38, 0.57)	0.61
Vessel density (%)	3,85	2,5	0.63 (0.45, 0.63)	0.61
Epidermal thickness (µm)	29	27	0.52 (0.33, 0.52)	0.84

95% CI: 95% confidence interval; OCTA: optical coherence tomography angiography; DEJ: dermal epidermal junction; PPC: polycyclic papillary contours; Hb: deoxygenized haemoglobin content (veins); HbO$_2$: deoxygenized haemoglobin content (arteries).
*Novel features not previously identified in the literature.
Features that separate malignant from benign tumours with significant diagnostic accuracy, *p*-adjusted < 0.05, are shown in bold.

n = 1. See Appendix S2 for dermoscopy images of all included lesions and Appendix S3 for patient demographics and body location of lesions. In total, skin biopsies from 39 of 41 lesions were sent for histopathological analysis. A subungual haematoma that later cleared, and a clinically evident seborrhoeic keratosis, were not biopsied. The selected lesions, according to histopathological assessment, included: 4 MM, 4 naevi with atypical intraepidermal melanocytic proliferation (AN), 5 keratinocyte carcinomas (1 SCC, 4 BCC), and 2 AK. The diagnoses for the remaining 26 lesions were benign and included 5 seborrhoeic keratosis, 15 naevi (dermal, junctional, compound and halo) and 6 other lesions, such as onychomycosis, haematoma, or inflammation. Scanning time for each patient was 22–35 min for all 5 scans, including dermoscopy and clinical photography.

Diagnostic features assessed by reflectance confocal microscopy, optical coherence tomography, photoacoustic imaging and high-frequency ultrasound

All evaluated features are reported in Table I. Features that separate malignant from benign tumours with significant diagnostic accuracy, *p*-adjusted < 0.05, are shown in bold. No HFUS features showed statistical significance. The most important findings for each scanning modality are presented in the following text, categorized into cell and skin architecture, molecular contrast and blood vessel characteristics.

Concerning data scatter of the images that were selected for further morphological analysis and diagnostic accuracy evaluation; 2–3 OCT images and 3–4 PAI images were recorded for each lesion and 1 image, with the lowest degree of movement artefacts, air trapping under the lens, etc., was selected. Regarding RCM images, the entire set of images was analysed, except for images with many artefacts from bubbles of oil under the lens or hairs, since they all represented parts of the lesion.

Photoacoustic imaging: morphological features. Dense superficial melanin was found frequently in both malignant and benign lesions and had low diagnostic impact, with a specificity of only 4% (Fig. S1). Overall, melanin distribution in the tumours was not a significant predictor for malignancy when used alone; however, together with information about vascularization, it has diagnostic abilities.

Photoacoustic imaging: blood vessel characteristics. Three important PAI features were significantly correlated with malignancy. A strong predictor for malignancy was abundant blood vessels inside the tumour area where blood vessels with oxygenated haemoglobin (HbO_2,), arteries, showed statistical significance with diagnostic accuracy 0.74 (95% CI 0.58, 0.87), *p*-adjusted = 0.02, whereas blood vessels with deoxygenated Hb (veins) showed a diagnostic accuracy 0.69 (95% CI 0.52, 0.83), *p*-adjusted = 0.08. A converging and chaotic network of blood vessels and melanin was demonstrated in most malignant lesions, as well as in AN. This feature is de-

picted in **Figs 1–3**. In addition, HbO_2 vessels outside the tumour were also associated with malignancy, although with low diagnostic accuracy 0.31 (95% CI 0.17, 0.48) *p*-adjusted = 0.08. Furthermore, most malignant tumours showed increased blood vessel diameter compared with benign lesions with high diagnostic accuracy for veins (Hb), 0.74 (95% CI 0.58, 0.87), *p*-adjusted = 0.02 and lower for arteries (HbO_2), where diagnostic accuracy was 0.51 (95% CI 0.35, 0.68), *p*-adjusted = 1.

Reflectance confocal microscopy: morphological features. This study confirmed well-known diagnostic RCM features, but also highlighted new ones. Six features were strongly associated with malignancy with a specificity of 100%; atypical melanocytes inside hair follicles/adnexa, found exclusively in MMs; and peritumoural dark clefting, peripheral palisading, dark islands, cauliflower-
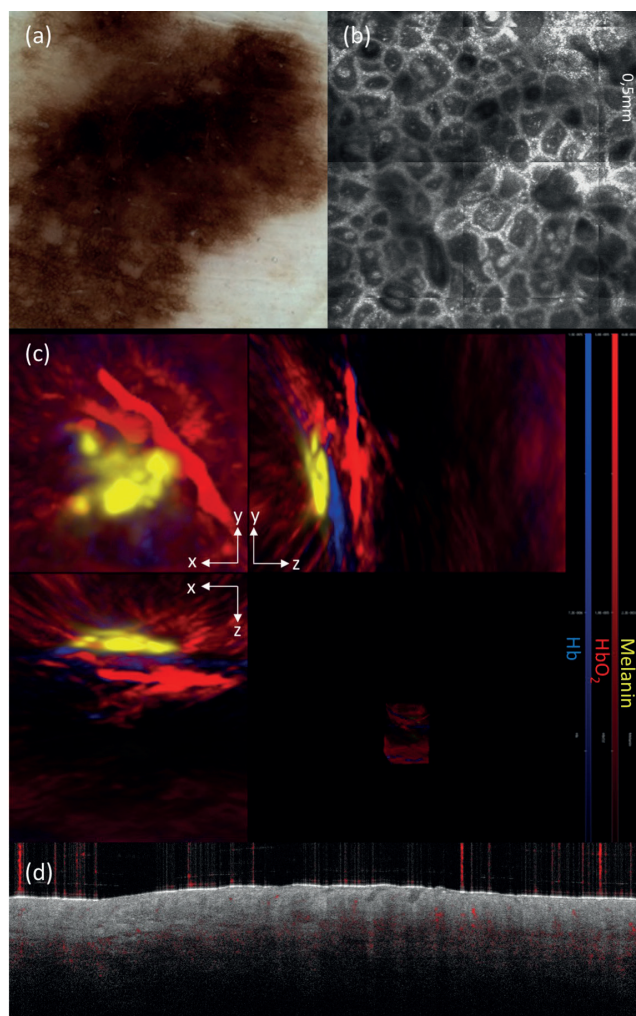

Fig. 1. Naevus with atypical proliferation. (a) Dermoscopy image. (b) Reflectance confocal microscopy: nests of melanocytes, slightly irregular edged papillae and nucleated cells inside dermal papillae. (c) Photoacoustic imaging: chaotic and prominent blood vessels outside melanin area (*yellow*). HbO_2 (*red*) and Hb (*blue*) blood vessels with enlarged diameter. (d) Optical coherence tomography: a marble-like epidermis with different shades of grey is visible and increased vascularization is recognized at depth of 0.5–1 mm (*red*).
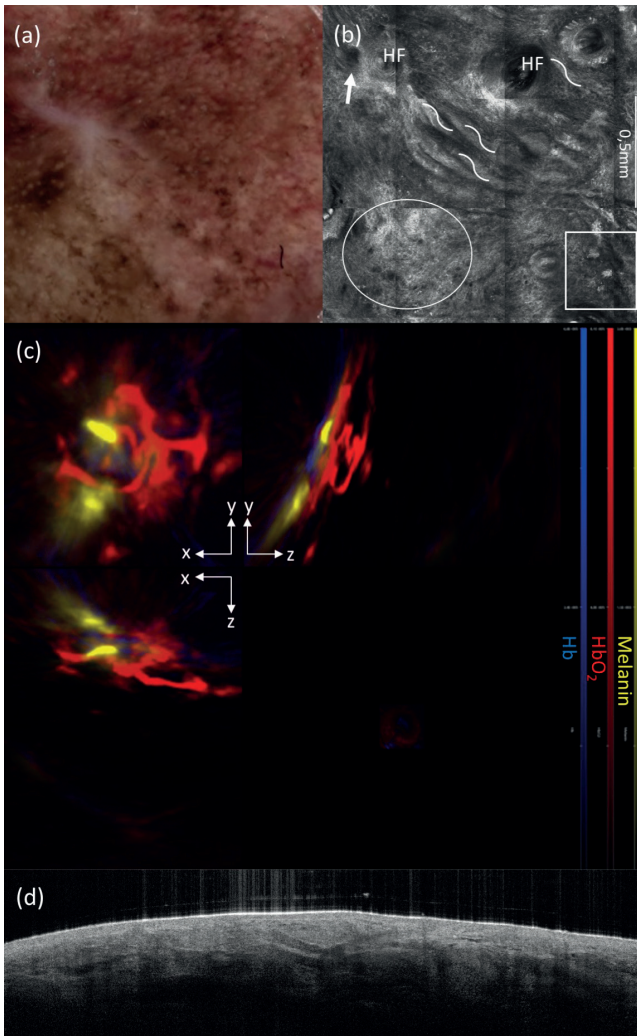
Fig. 2. Lentigo maligna melanoma. (a) Dermoscopy image. (b) Reflectance confocal microscopy: dermal-epidermal junction with pagetoid spread (*square*), non-edged papillae (*arrow*), cordlike cell aggregations (*waves*), atypical melanocytes inside hair follicles (HF) and atypical honeycomb pattern (*circle*). (c) Photoacoustic imaging: blood vessels (HbO$_2$ red and Hb *blue*) inside tumour and a converging network of blood vessels and melanin (*yellow*) and abundant HbO$_2$ signal with increased diameter outside tumour. (d) Optical coherence tomography: homogeneous signal from epidermis and more heterogenous signal from upper dermis and white strands of fibrosis appear, corresponding to the scar seen on the dermoscopy image.

Fig. 3. Basal cell carcinoma. (a) Dermoscopy image. (b) Reflectance confocal microscopy: dark tumour islands (*), streaming of keratinocytes (*arrows*) and slightly atypical honeycomb pattern (*circles*). (c) Photoacoustic imaging: abundant HbO$_2$ signal (red) inside melanin area, demonstrating a converging network of melanin (*yellow*), HbO2 and Hb (*blue*). (d) Optical coherence tomography: ovoid dark basal cell carcinoma islands and increased blood flow below and inside the tumour (*red*).

like lesions and streaming found in BCCs (see Fig. 3 illustrating a BCC lesion). Frequently observed in MMs and ANs were features such as pagetoid spread with dendritic and round cells, non-edged papillae and nucleated cells in dermal papillae, all with *p*-adjusted <0.05 (see Figs 1 and 2 for images of MM and AN, respectively). Cordlike cell aggregations in dermis were significantly associated with malignancy, with a diagnostic accuracy of 0.73 (95% CI 0.57, 0.86), *p*-adjusted=0.02. Overall, a homogeneous epidermis, characterized by a regular honeycombed pattern, was strongly correlated with benign lesions, with a diagnostic accuracy of 0.22 (95% CI 0.11, 0.38), *p*-adjusted=0.01, and with a low specificity of only 8%. Correspondingly, an atypical honeycomb
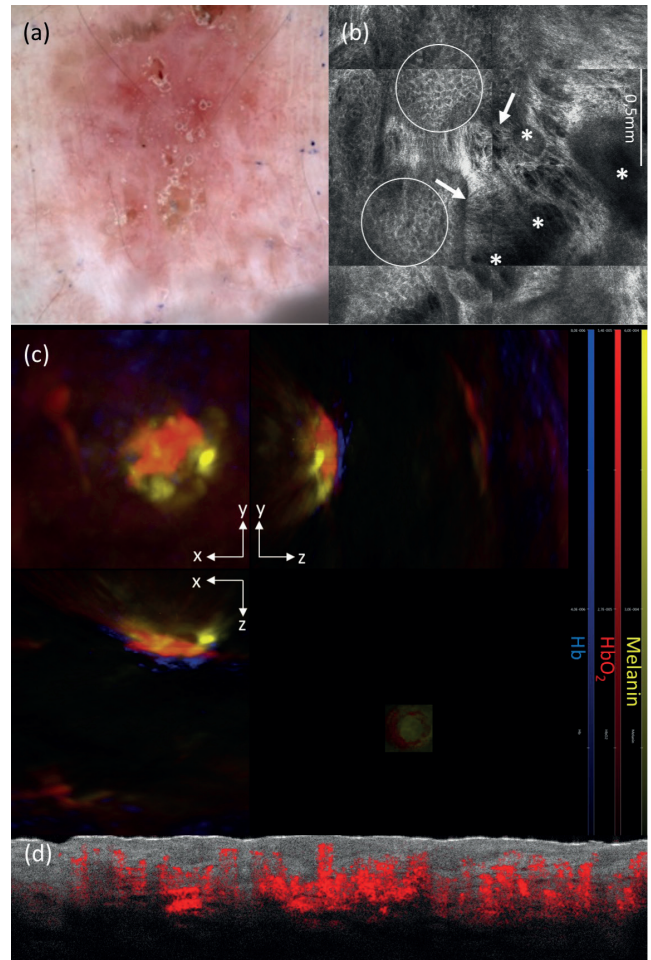
pattern, composed of dysplastic cells, was significantly associated with malignancy, with a specificity of 81% and a diagnostic accuracy of 0.76 (95% CI 0.6, 0.88), *p*-adjusted=0.02.

Reflectance confocal microscopy: blood vessel characteristics. Arborizing vessels in RCM images were significantly associated with malignancy, predominantly expressed in BCCs, with a diagnostic accuracy of 0.78 (95% CI 0.62, 0.89), *p*-adjusted=0.01 and specificity of 100%. Vasculature inside the tumour and an enlarged diameter of blood vessels were more frequently found in malignant lesions compared with benign lesions, but without high diagnostic accuracy.

Commercial optical coherence tomography and ultra-high resolution optical coherence tomography: morphological features. Due to the COVID-19 pandemic restrictions some scans could not be performed by the Technical University of Denmark (DTU), and this OCT data is missing from the analysis. Clefting, a characteris-

tic for BCC, was strongly associated with malignancy, with a specificity of 100%, both with commercial OCT (C-OCT), with a diagnostic accuracy of 0.73 (95% CI 0.57, 0.86), *p*-adjusted = 0.02; and ultra-high resolution OCT (UHR-OCT), with a diagnostic accuracy of 0.71 (95% CI 0.52, 0.86), *p*-adjusted = 0.08. Ovoid dark areas, shown in Fig. 3, were observed in all BCCs and were significantly associated with malignancy in C-OCT with a specificity of 96%, a diagnostic accuracy of 0.71 (95% CI 0.54, 0.84), *p*-adjusted = 0.04. A marble-like epidermis, illustrated in Fig. 1, is a novel feature described by our group, found in ANs and MMs. However, the diagnostic accuracy was low, and marble-like epidermis could not be used as an indicator of malignancy.

Commercial optical coherence tomography and ultra-high resolution optical coherence tomography: blood vessel characteristics. Most malignant lesions were characterized by a larger blood vessel diameter and by more blood vessels in the 3D scan, corresponding to a larger volume of blood vessels per mm3, and here referred to as density, compared with benign lesions. This is illustrated in **Fig. 4**, where MM was prominently associated with greater vessel diameter and density, compared with all other lesions. Furthermore, a more superficial blood vessel plexus depth was associated with malignant lesions, with a mean plexus depth of 275 µm (95% CI 223, 307), compared with benign lesions 289 µm (95% CI 262, 352). However, diagnostic accuracies for blood vessel features were not high enough to discriminate between malignant and benign lesions, with an AUC of 0.57–0.63. Vessel density showed the highest separation capacity, with an AUC of 0.63 (95% CI 0.45, 0.63), as outlined in Fig. 4c.

High-frequency ultrasound: morphological features. No features assessed by HFUS had sufficient diagnostic
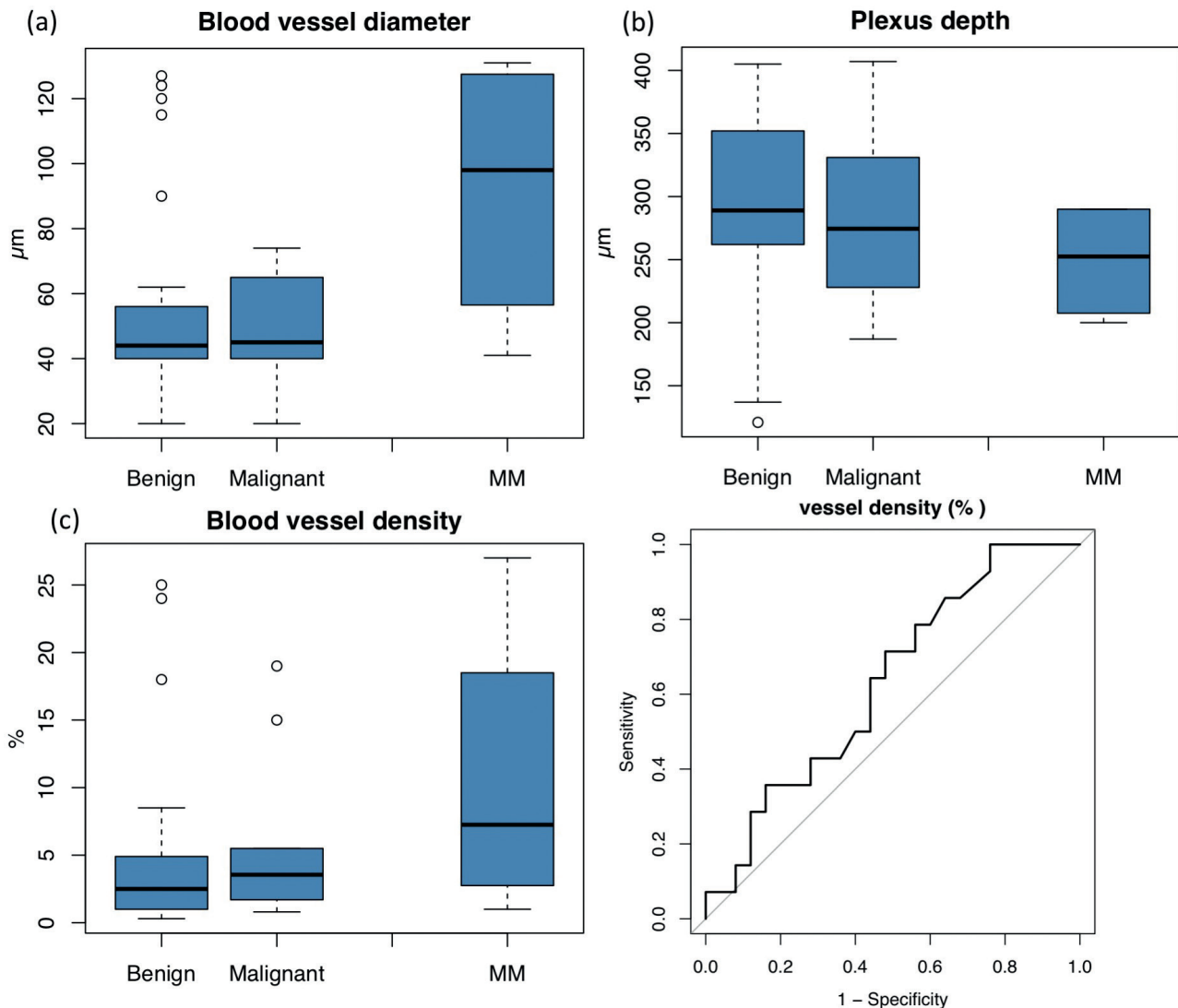

Fig. 4. Angiographic optical coherence tomography (OCTA). Blood vessel diameter, density and plexus depth in malignant/premalignant lesions, malignant melanoma (MM) and benign lesions. Boxplot showing: (a) larger vessel diameter in malignant lesions compared with benign lesion, prominently associated with MM; (b) a more superficial plexus depth in malignant lesions and MM; (c) greater vessel density in malignant lesions and MM compared with benign lesions, visualized in boxplots and receiver operating characteristic (ROC) curve.

accuracy to discriminate malignant from benign lesions. Dark hypoechogenic areas were commonly encountered in all lesions and were not specific to malignant tumours.

High-frequency ultrasound: blood vessel characteristics. HFUS blood vessel characteristics assessed in Doppler mode, were not able to discriminate benign from malignant lesions.

Tumour thickness measured with optical coherence tomography, photoacoustic imaging and high-frequency ultrasound

Not surprisingly, no significant difference was found in tumour thickness between benign and malignant lesions measured with HFUS, the 2 different OCT systems and PAI (see Table SI), which allows comparison between blood vessels in benign and malignant tumours. Thickness measurements were not compared with histology.

DISCUSSION

This study explored image features with previously known high diagnostic impact, as well as novel features described by our group for this study. Previous studies of RCM and OCT have shown high diagnostic sensitivity and specificity for, especially, MM and BCC (22, 27, 30). No statistically significant diagnostic accuracies exceeding 0.78 were found. This is reflected in the finding that very high sensitivities were matched by low specificity and vice versa. This pilot study in a University Hospital setting included patients consecutively during their first clinical visit when local dermatologists were closed due to Covid-19 restrictions, and this will invariably result in lower specificity and sensitivity. However, it provides a more realistic picture of the diagnostic accuracy of the scanners in daily clinical practice, where multiple types of pigmented lesions are encountered. The fact that high specificity was seen alongside a low sensitivity and vice versa highlights the relevance of combining, especially, PAI, OCT and RCM in the future, to potentially obtain valuable complementary effects of multiple technologies in a single session.

Of interest was superficial blood vessel morphology demonstrated with OCTA. Recent studies have demonstrated that OCTA evaluation of blood vessel morphology can be used for diagnosis and margin delineation in MMs and BCCs (14, 31). In the current study malignant lesions expressed a more superficial plexus depth with OCTA. Although the separation capacity in determining malignant vs benign pigmented skin tumours was found to be low for all vascular features analysed by C-OCT, an AUC of 0.6 (95% CI 0.4, 0.6), a clear pattern was identified.

PAI is cutting edge among non-invasive technologies for skin imaging, and has been used as a pre-surgical tool for delineation of MMs and BCCs (18, 19, 32). Benign lesions tended to have a denser superficial melanin distribution, but this characteristic feature needs further investigation. The current study found that a converging network of blood vessels and melanin was strongly associated with malignancy. Abundant blood vessels inside the tumour area were found in most malignant tumours.

The current study showed that 12 RCM features, characterizing cells and skin architecture, were independently and significantly associated with malignancy by means of statistical analysis. A regular honeycomb was the single feature found to be specific for benign lesions. The only feature related to vascularity that showed significant diagnostic accuracy with RCM was arborizing vessels. RCM image analysis is operator dependent, and many of the image features were found both in benign and malignant lesions, making exclusive RCM application in diagnosis less effective.

Differential diagnosis of pigmented skin lesions with OCT alone seems difficult, as the resolution of OCT does not enable visualization of single cells. Schuh et al. (5) showed that different OCT systems may provide quite different images of BCC lesions. In the current study using 2 different OCT devices, 1 commercial and 1 prototype with ultra-high resolution, 2 complementary sets of data were obtained. The OCT features carrying high diagnostic impact were "clefting" and "ovoid dark areas". This correlates with previous findings and makes OCT a relevant tool in BCC diagnosis and margin assessment (16, 17). A new feature presented in this study is "marble-like epidermis", which seems to be specific for MMs and ANs. However, larger studies are needed to fortify its diagnostic accuracy. While several features have been associated with particular diagnoses in previous studies; for example, icicle-shaped structures/ice peaks (22), these were not demonstrated in the current study data as diagnostically important. Reassuringly, marble-like epidermis can be considered a variant of icicle shapes, since it also refers to different vertical shades of grey in the epidermis.

HFUS did not contribute with any significant features or qualities that could be used for diagnosis in this study, which is expected due to low resolution.

Overall, no significant difference was found in tumour thickness between benign and malignant lesions. This strengthens the ability of PAI and OCT to discriminate blood vessels between malignant and benign lesions, as the vascular variance cannot be explained by differences in tumour thickness.

This prospective pilot study has some limitations. Because of the ongoing Covid-19 pandemic the patient number was smaller than expected. Nevertheless, apart from halting many clinical studies, delays in presentation due to Covid-19 have also caused an alarming backlog of superficial MM and the substantial healthcare burden of ruling out malignancy in suspicious pigmented lesions (33), highlighting the great potential for novel non-invasive imaging methods in the future.

Lastly, portable and economical systems are in demand, in order to achieve widespread adoption of

advanced imaging modalities in the clinic. Currently, utilizing multiple imaging technologies is costly; however, this must be considered in comparison with the rapid development of cheaper lasers, and in comparison with the burden that unnecessary biopsies, misdiagnosis, or surgical excision of benign tumours places on the healthcare system (34).

In conclusion, based on rapid image-guided evaluation of cell morphology, skin architecture, melanin content, and blood vessels, it is possible to differentiate malignant from benign pigmented lesions with significant diagnostic accuracy. High specificity was often seen in conjunction with low sensitivity, and vice versa, which prompts a complementary effect of combining OCT, RCM and PAI at the bedside in future studies of diagnosis of suspicious pigmented skin tumours.

With increasing incidences of skin cancer worldwide there is a great need for non-invasive imaging tools that can effectively capture malignant tumours at an early stage. Based on this pilot study, there is reason to foresee a valuable clinical applicability of OCT, RCM and PAI in combination, facilitating rapid diagnosis of suspicious pigmented skin tumours. The significant, but moderate, diagnostic accuracy can potentially decrease delay from diagnosis to treatment in the future.

REFERENCES

1. Giuffrida R, Conforti C, Di Meo N, Deinlein T, Guida S, Zalaudek I. Use of noninvasive imaging in the management of skin cancer. Curr Opin Oncol 2020; 32: 98–105.
2. Malvehy J, Hauschild A, Curiel-Lewandrowski C, Mohr P, Hofmann-Wellenhof R, Motley R, et al. Clinical performance of the Nevisense system in cutaneous melanoma detection: an international, multicentre, prospective and blinded clinical trial on efficacy and safety. Br J Dermatol 2014; 171: 1099–1107.
3. Marghoob AA, Swindle LD, Moricz CZ, Sanchez Negron FA, Slue B, Halpern AC, et al. Instruments and new technologies for the in vivo diagnosis of melanoma. J Am Acad Dermatol 2003; 49: 777–797; quiz 798–779.
4. Mogensen M, Jemec GB. Diagnosis of nonmelanoma skin cancer/keratinocyte carcinoma: a review of diagnostic accuracy of nonmelanoma skin cancer diagnostic tests and technologies. Dermatol Surg 2007; 33: 1158–1174.
5. Schuh S, Kaestle R, Sattler E, Welzel J. Comparison of different optical coherence tomography devices for diagnosis of non-melanoma skin cancer. Skin Res Technol 2016; 22: 395–405.
6. Ulrich M. Optical coherence tomography for diagnosis of basal cell carcinoma: essentials and perspectives. Br J Dermatol 2016; 175: 1145–1146.
7. Kadouch DJ, van Haersma de With ASE, Elshot YS, Peppelman M, Bekkenk MW, Wolkerstorfer A, et al. Interrater and intrarater agreement of confocal microscopy imaging in diagnosing and subtyping basal cell carcinoma. J Eur Acad Dermatol Venereol 2018; 32: 1278–1283.
8. Bobadilla F, Wortsman X, Muñoz C, Segovia L, Espinoza M, Jemec GB. Pre-surgical high resolution ultrasound of facial basal cell carcinoma: correlation with histology. Cancer Imaging 2008; 8: 163–172.
9. Machet L, Belot V, Naouri M, Boka M, Mourtada Y, Giraudeau B, et al. Preoperative measurement of thickness of cutaneous melanoma using high-resolution 20 MHz ultrasound imaging: a monocenter prospective study and systematic review of the literature. Ultrasound Med Biol 2009; 35: 1411–1420.
10. Haroon A, Shafi S, Rao BK. Using Reflectance confocal microscopy in skin cancer diagnosis. Dermatol Clin 2017; 35: 457–464.
11. Sahu A, Yélamos O, Iftimia N, Cordova M, Alessi-Fox C, Gill M, et al. Evaluation of a combined reflectance confocal microscopy-optical coherence tomography device for detection and depth assessment of basal cell carcinoma. JAMA Dermatol 2018; 154: 1175–1183.
12. Alawi SA, Kuck M, Wahrlich C, Batz S, McKenzie G, Fluhr JW, et al. Optical coherence tomography for presurgical margin assessment of non-melanoma skin cancer – a practical approach. Exp Dermatol 2013; 22: 547–551.
13. Israelsen NM, Maria M, Mogensen M, Bojesen S, Jensen M, Haedersdal M, et al. The value of ultrahigh resolution OCT in dermatology – delineating the dermo-epidermal junction, capillaries in the dermal papillae and vellus hairs. Biomed Opt Express 2018; 9: 2240–2265.
14. Themstrup L, De Carvalho N, Nielsen SM, Olsen J, Ciardo S, Schuh S, et al. In vivo differentiation of common basal cell carcinoma subtypes by microvascular and structural imaging using dynamic optical coherence tomography. Exp Dermatol 2018; 27: 156–165.
15. Themstrup L, Banzhaf CA, Mogensen M, Jemec GB. Optical coherence tomography imaging of non-melanoma skin cancer undergoing photodynamic therapy reveals subclinical residual lesions. Photodiagnosis Photodyn Ther 2014; 11: 7–12.
16. De Carvalho N, Schuh S, Kindermann N, Kästle R, Holmes J, Welzel J. Optical coherence tomography for margin definition of basal cell carcinoma before micrographic surgery-recommendations regarding the marking and scanning technique. Skin Res Technol 2018; 24: 145–151.
17. Mogensen M, Joergensen TM, Nürnberg BM, Morsy HA, Thomsen JB, Thrane L, et al. Assessment of optical coherence tomography imaging in the diagnosis of non-melanoma skin cancer and benign lesions versus normal skin: observer-blinded evaluation by dermatologists and pathologists. Dermatol Surg 2009; 35: 965–972.
18. Attia ABE, Balasundaram G, Moothanchery M, Dinish US, Bi R, Ntziachristos V, et al. A review of clinical photoacoustic imaging: current and future trends. Photoacoustics 2019; 16: 100144.
19. Chuah SY, Attia ABE, Ho CJH, Li X, Lee JS, Tan MWP, et al. Volumetric multispectral optoacoustic tomography for 3-dimensional reconstruction of skin tumors: a further evaluation with histopathologic correlation. J Invest Dermatol 2019; 139: 481–485.
20. Chen Z, Rank E, Meiburger KM, Sinz C, Hodul A, Zhang E, et al. Non-invasive multimodal optical coherence and photoacoustic tomography for human skin imaging. Sci Rep 2017; 7: 17975.
21. Breathnach A, Concannon E, Dorairaj JJ, Shaharan S, McGrath J, Jose J, et al. Preoperative measurement of cutaneous melanoma and nevi thickness with photoacoustic imaging. J Med Imaging (Bellingham) 2018; 5: 015004.

22. Garbarino F, Migliorati S, Farnetani F, De Pace B, Ciardo S, Manfredini M, et al. Nodular skin lesions: correlation of reflectance confocal microscopy and optical coherence tomography features. J Eur Acad Dermatol Venereol 2020; 34: 101–111.

23. Hoogedoorn L, Peppelman M, Blokx WA, van Erp PE, Gerritsen MJ. Prospective differentiation of clinically difficult to distinguish nodular basal cell carcinomas and intradermal nevi by non-invasive reflectance confocal microscopy: a case series study. J Eur Acad Dermatol Venereol 2015; 29: 330–336.

24. Oliveira A, Zalaudek I, Arzberger E, Hofmann-Wellenhof R. Seborrhoeic keratosis imaging in high-definition optical coherence tomography, with dermoscopic and reflectance confocal microscopic correlation. J Eur Acad Dermatol Venereol 2017; 31: e125–e127.

25. Fredman G, Qiu Y, Ardigò M, Mogensen M. Skin tags imaged by reflectance confocal microscopy, optical coherence tomography and multispectral optoacoustic tomography at the bedside. Skin Res Technol 2021; 27: 324–331.

26. Guitera P, Pellacani G, Crotty KA, Scolyer RA, Li LX, Bassoli S, et al. The impact of in vivo reflectance confocal microscopy on the diagnostic accuracy of lentigo maligna and equivocal pigmented and nonpigmented macules of the face. J Invest Dermatol 2010; 130: 2080–2091.

27. Dinnes J, Deeks JJ, Saleh D, Chuchu N, Bayliss SE, Patel L, et al. Reflectance confocal microscopy for diagnosing cutaneous melanoma in adults. Cochrane Database Syst Rev 2018; 12: Cd013190.

28. Rocha L, Vilain RE, Scolyer RA, Lo SN, Drummond M, Star P, et al. Confocal microscopy, dermoscopy, and histopathology features of atypical intraepidermal melanocytic proliferations associated with evolution to melanoma in situ. Int J Dermatol 2022; 61: 167–174.

29. Benjamini Y, Hochberg Y. Controlling the false discovery rate: a practical and powerful approach to multiple testing. J R Statist Soc B 1995; 57: 289–300.

30. Dinnes J, Deeks JJ, Chuchu N, Saleh D, Bayliss SE, Takwoingi Y, et al. Reflectance confocal microscopy for diagnosing keratinocyte skin cancers in adults. Cochrane Database Syst Rev 2018; 12: Cd013191.

31. De Carvalho N, Welzel J, Schuh S, Themstrup L, Ulrich M, Jemec GBE, et al. The vascular morphology of melanoma is related to Breslow index: an in vivo study with dynamic optical coherence tomography. Exp Dermatol 2018; 27: 1280–1286.

32. von Knorring T, Mogensen M. Photoacoustic tomography for assessment and quantification of cutaneous and metastatic malignant melanoma – a systematic review. Photodiagnosis Photodyn Ther 2021; 33: 102095.

33. Welch HG, Mazer BL, Adamson AS. The rapid rise in cutaneous melanoma diagnoses. N Engl J Med 2021; 384: 72–79.

34. Guy GP, Jr., Machlin SR, Ekwueme DU, Yabroff KR. Prevalence and costs of skin cancer treatment in the U.S., 2002–2006 and 2007–2011. Am J Prev Med 2015; 48: 183–187.